Reviews of Electromagnetics, Vol. V, 2026
EuCAP 2026 Special Issue
DOI: 10.53792/RoE/2026/26001

Reviews of Electromagnetics
EuCAP 2026 Special Issue

Modal-Domain Design of Layered Multiport Waveguide Crossings Based on Transformation Optics

Nona Messhenas[1]*, Werner L. Schroeder[1], Thomas Kaiser[2]

Abstract
A systematic design methodology for transformation-optics-derived two-dimensional graded-index dielectric structures at millimeter-wave frequencies is presented using a modal-domain formulation. Instead of prescribing a bulk spatial permittivity distribution, the proposed approach specifies the local propagation velocity of the fundamental guided TE_0 slab mode, yielding an equivalent spatial distribution of modal effective refractive index. The Maxwell's fish-eye profile derived from transformation optics is mapped onto a layered dielectric configuration composed of mirror-symmetric two-material stacks selected from a precomputed lookup library. The approach explicitly considers fabrication-compatible layered realizations based on available dielectric materials and planar multilayer manufacturing constraints, ensuring compatibility with low-loss dielectric waveguide structures. An eight-port dielectric waveguide crossing operating at 77 GHz is used as a representative design example. Full-wave simulations indicate efficient transmission of the fundamental mode over the operating band, low crosstalk levels, and negligible higher-order mode conversion. The influence of dielectric loss and geometric design parameters is also investigated, confirming robust behavior under realistic material conditions. Compared with the preliminary conference contribution, this work introduces the modal-domain formulation, the layered dielectric synthesis strategy, and an extended performance analysis for multiport configurations. The presented framework provides a systematic approach for fabrication-compatible layered realizations of transformation-optics-derived guided-wave devices and supports scalable dielectric waveguide interconnects for 77 GHz automotive radar systems.

Key terms
Millimeter-wave; dielectric waveguides; layered dielectric structures; gradient index; transformation optics; Maxwell's fish-eye lens; multiport waveguide crossings

[1] *Department of RF and EMC Systems, RheinMain University of Applied Sciences, Rüsselsheim am Main, Germany*
[2] *Department of Electrical Engineering and Information Technology, University of Duisburg-Essen, Duisburg, Germany*
*__Corresponding author__: nona.messhenas@hs-rm.de

Received: 24/05/2026, Accepted: 29/10/2026, Published: 10/11/2026

1. Introduction

Millimeter-wave systems operating in the 77 GHz band are widely deployed in automotive radar and high-resolution short-range sensing, where compact front-ends and dense antenna arrays support beamforming and multi-channel operation [1]- [2]. As antenna counts increase and array apertures become electrically larger, guided-wave interconnects between transceiver modules and radiating elements becomes a critical design consideration. In particular, interconnect attenuation, phase imbalance, and undesired electromagnetic interactions can degrade radar sensitivity and angular resolution, motivating compact and scalable routing solutions for millimeter-wave front-ends. High-density guided-wave routing also arises in passive array architectures such as retro-reflective Van Atta configurations [3]- [4], where multiple signal paths must be routed while maintaining well-controlled phase relationships. At 77 GHz, the realization of such interconnect networks becomes increasingly challenging due to dielectric and radiation losses, as well as tight fabrication tolerance in compact layouts, particularly when multiple crossings or dense routing regions are required.

In this context, fully dielectric multilayer realizations represent a promising approach for passive millimeter-wave components. Rectangular dielectric waveguides (RDWGs) and related

guiding structures have demonstrated low-loss transmission in the 60–100 GHz range [5], providing a pathway toward compact guided-wave routing without relying on metallic interconnect structures. Layered dielectric configurations further enable permittivity-engineered designs within manufacturable multilayer stacks and support the realization of complex guided-wave geometries at millimeter-wave frequencies.

Waveguide crossings based on graded-index concepts have been extensively investigated in the optical domain, where fully dielectric implementations are enabled by high-index-contrast materials and fine subwavelength patterning techniques [6]-[7]. In particular, Maxwell's fish-eye (MFE) profiles [8], interpreted within the framework of transformation optics (TO), have been employed to realize compact multiport crossings with low crosstalk in integrated photonic platforms. These studies demonstrate the effectiveness of graded-index distributions for guided-wave routing in dielectric media.

At millimeter-wave frequencies, however, direct translation of such optical implementations is not straightforward. Available dielectric materials provide limited permittivity contrast and exhibit non-negligible loss tangents, while achievable feature sizes and layer thicknesses are constrained by practical fabrication tolerances. Subwavelength patterning approaches commonly used at optical frequencies are therefore not well suited for scalable multilayer manufacturing at 77 GHz. Earlier MFE-based realizations relying on variation of total slab thickness resulted in taper-like geometries susceptible to radiation loss and increased fabrication complexity. These limitations motivate realizations that preserve the focusing behavior of the MFE profile while remaining compatible with manufacturable layered dielectric waveguide structures.

Previous studies considered idealized MFE-based multiport crossings and preliminary layered realizations based on modal-domain concepts [9, 10]. Building on these results, the present work combines the TO-based modal formulation with a fully layered eight-port dielectric waveguide crossing at 77 GHz and presents a comprehensive full-wave evaluation of transmission characteristics, crosstalk, modal conversion, and selected geometric design parameters.

To this end, a modal-domain formulation is employed for the layered realization of a dielectric MFE-based multiport waveguide crossing at 77 GHz. Rather than prescribing a bulk spatial permittivity distribution, the formulation specifies the local phase velocity experienced by the fundamental guided slab mode, thereby defining a spatial distribution of modal effective refractive index. This target profile is approximated using mirror-symmetric two-material dielectric layer stacks selected from a precomputed lookup library and assigned cell-wise, resulting in a geometry compatible with multilayer fabrication and dielectric additive manufacturing.

An eight-port waveguide crossing serves as a representative example. Full-wave simulations demonstrate low insertion loss of the dominant guided mode, suppressed higher-order mode excitation, stable phase symmetry between opposing ports, and low crosstalk levels across the operating band. In addition, a measurement-oriented configuration with parallel metallic plates confirms that the proposed structure maintains its performance under physically realizable conditions. These results identify MFE-based dielectric waveguide crossings as compact and scalable guided-wave routing solutions for millimeter-wave automotive radar front-ends and related systems.

2. Concept and Design Methodology

2.1. Maxwell's Fish-eye Principle

The Maxwell's fish-eye (MFE) profile, originally proposed by J. C. Maxwell based on ray-optics considerations [8], is a dielectric sphere of radius R whose refractive index varies according to

$$n_w(r) = \frac{n_{\max}}{1 + \left(\frac{r}{R}\right)^2}, \tag{1}$$

where $n_{\max}$ denotes the maximum refractive index at the center and r is the radial coordinate.

A key property of this profile is its point-to-point imaging behavior: rays launched from a boundary point follow curved trajectories and reconverge at the diametrically opposite point with equal optical path length. The same property also applies in two dimensions for a circular cylindrical implementation of (1), where r and R are interpreted with respect to the cylinder axis.

Beyond its classical role as an imaging medium, the MFE profile is attractive for waveguide crossings. The equal-path-length property promotes symmetric phase transfer between opposing ports, while the smooth refractive-index gradient guides energy without abrupt discontinuities that would otherwise increase reflections in conventional junctions. When truncated and integrated into a multiport interface, the MFE region therefore provides a natural routing mechanism between designated input and output ports while suppressing crosstalk toward neighboring ports.

2.2. Transformation Optics and Conformal Mapping

The point-to-point imaging property discussed above is suggestive of the behavior required in a planar waveguide crossing. Practical crossings, however, do not launch isolated rays but guided modes whose transverse field distributions must be transferred from an input port to the corresponding output port. A purely cylindrical two-dimensional MFE profile therefore cannot be employed directly without geometric adaptation.

To obtain a geometry compatible with multiple planar ports, the MFE profile is reshaped while preserving its optical path properties. Following related concepts in [11], a transformation-optics (TO) framework [12, 13] is used to map the circular virtual domain of the ideal MFE lens onto a regular polygonal domain suitable for port attachment.

Only a two-dimensional transformation is required here. Since general coordinate transformations lead to anisotropic material responses [14], attention is restricted to conformal mappings, which preserve local angles and therefore permit an isotropic equivalent medium. This avoids tensor-valued material parameters and simplifies physical realization.

Let the original MFE medium reside in a *virtual domain* parameterized by the complex coordinate w, with refractive index distribution $n_w(w)$. The goal is to map this domain into a *physical domain* described by the complex coordinate $p = x + \mathrm{j}\,y \in \mathbb{C}$,

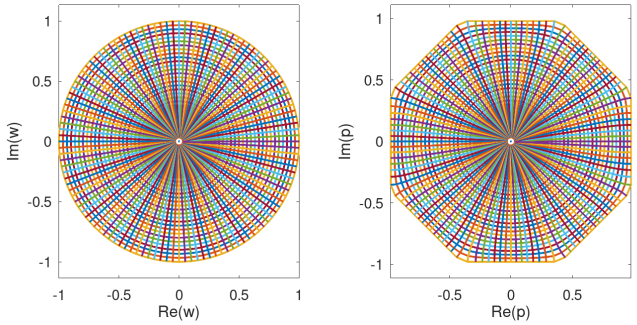


Figure 1: Illustration of the conformal mapping (3) for $N = 8$.

whose boundary conforms to the desired polygonal geometry suitable for port attachment. Under a conformal mapping $p = p(w)$, the transformed refractive index in the physical domain becomes [14]

$$n_p(p(w)) = \left| \frac{\mathrm{d}p(w)}{\mathrm{d}w} \right|^{-1} n_w(w). \tag{2}$$

This transformation preserves the optical path lengths of the virtual medium while reshaping the domain into the required polygonal cross-section. In this manner, the focusing behavior of the MFE is retained, but the geometry is adapted to the multiport configuration needed for a waveguide crossing.

Among several possible mappings, the SCHWARZ–CHRISTOFFEL transformation [15] from the unit disk to the interior of a regular polygon is selected for its simplicity and numerical convenience. We approximate the integral

$$p(w) = C \int_{t=0}^{w} \prod_{i=1}^{N} (w_i - t)^{-\frac{2}{N}} \, \mathrm{d}t, \tag{3}$$

where, for $i = \{1, \ldots, N\}$, $w_i = \exp\left(\mathrm{j}\,\pi \frac{2i-1}{N}\right)$ is a *prevertex* and $C > 0$ a scaling factor. The simplicity of the formula is due to N-fold rotational symmetry in both domains. As a further advantage, the derivative in (2) is available in analytical form, viz.

$$\left| \frac{\mathrm{d}p(w)}{\mathrm{d}w} \right|^{-1} = \frac{1}{C} \left| \prod_{i=1}^{N} (w_i - w) \right|^{\frac{2}{N}}. \tag{4}$$

Fig. 1 illustrates the conformal mapping (3) for the case $N = 8$. This mapping is used below.

2.3. Layered Slab-Waveguide Approximation of the TO Medium

While the TO formulation yields an idealized continuous spatial permittivity distribution, practical realization requires discretization into manufacturable structures. In the present work, the TO-derived target profile is implemented through a layered representation defined by the modal effective index. The structure is modeled as a two-material multilayer slab medium, and the realization task is formulated as an assignment problem: for a prescribed spatial target distribution of effective permittivity $\varepsilon_{\mathrm{r,eff}}(x, y)$ associated with the fundamental slab-waveguide mode, suitable layer sequences are selected subject to practical layering constraints.

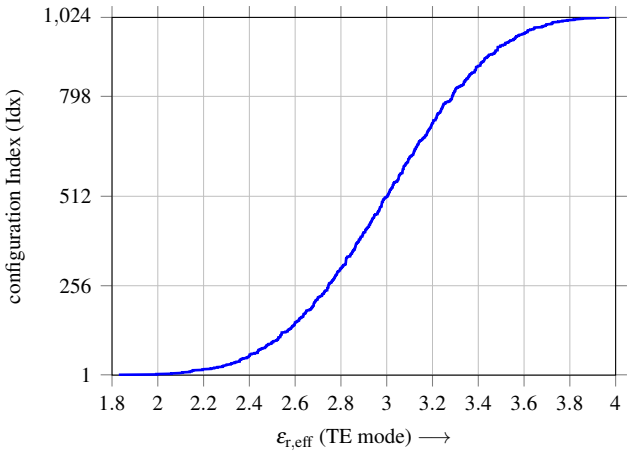


Figure 2: Effective relative permittivity $\varepsilon_{\mathrm{r,eff}}$ of all 2^{10} possible multilayer stacks composed of two dielectric materials ($\varepsilon_{\mathrm{r,L}} = 2.2$, $\varepsilon_{\mathrm{r,H}} = 4.5$). Each stack consists of 10 layers of equal thickness $t = 0.2\,\mathrm{mm}$, evaluated at 77 GHz.

Each spatial cell is modeled as an m-layer slab stack of uniform layer thickness t, resulting in a total height $h = mt$. Two low-loss dielectric materials are used: a low-index material L with relative permittivity $\varepsilon_{\mathrm{r,L}}$ and a high-index material H with relative permittivity $\varepsilon_{\mathrm{r,H}}$. A stacking sequence is denoted by $\mathbf{s} \in \{L, H\}^m$.

For each stack configuration $\mathbf{s}$, the propagation constant $\beta(\mathbf{s})$ of the fundamental guided mode is computed using a frequency-domain vector mode solver for multilayer slab waveguides (MLSWG) [16]. The corresponding effective relative permittivity experienced by the mode is defined as

$$\varepsilon_{\mathrm{r,eff}}(\mathbf{s}) = \left(\frac{\beta(\mathbf{s})}{k_0} \right)^2, \qquad k_0 = \frac{2\pi}{\lambda_0}, \tag{5}$$

where λ_0 denotes the free-space wavelength. This formulation establishes a direct and physically interpretable mapping between the stack geometry and the effective permittivity governing guided-wave propagation. The number of layers m governs both the resolution of achievable effective-permittivity values and the structural complexity. Increasing m enlarges the configuration library and improves approximation accuracy, but also increases fabrication sensitivity. For binary material selection, the total number of possible stacking sequences is 2^m. In the present work, $m = 10$ layers are selected as a practical compromise between effective-permittivity resolution and structural complexity.

Fig. 2 shows the effective relative permittivity $\varepsilon_{\mathrm{r,eff}}$ obtained for all 1024 layer configurations at $m = 10$, assuming a layer thickness of $t = 0.2$ mm, a low-permittivity material $\varepsilon_{\mathrm{r,L}} = 2.2$, and a high-permittivity material $\varepsilon_{\mathrm{r,H}} = 4.5$ at 77 GHz. The achievable values form an almost continuous range (≈ 1.82–3.97), bounded by the homogeneous low- and high-index stacks, while intermediate sequences densely populate the range. This confirms that smoothly varying GRIN profiles can be closely approximated using a finite library of layered stacks. In practice, a reduced subset $\mathscr{L}_m \subset \{L, H\}^m$ is selected to balance effective permittivity coverage and layout simplicity. Typical selection

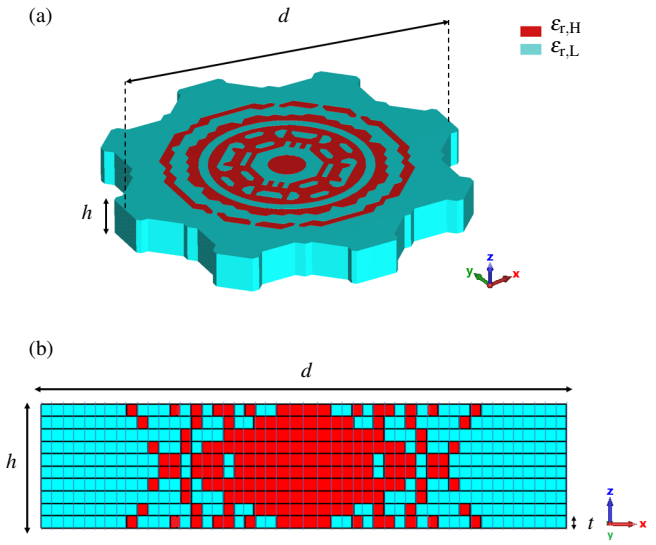


Figure 3: Conceptual geometry of the layered realization of TO-derived MFE core region. (a) Three-dimensional perspective view. (b) Cross-section at $y = 0$ through the MFE core.

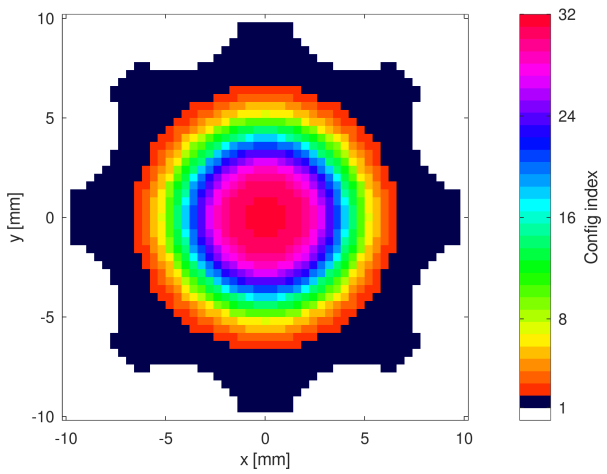


Figure 4: Spatial distribution of the layer-stack configuration indices at 77 GHz for the GRIN region in Fig. 3.

criteria include limiting the number of material interfaces, enforcing minimum run lengths of identical layers, and favoring mirror-symmetric stacks with respect to the slab mid-plane. For even m, this symmetry constraint reduces the number of distinct configurations to $2^{m/2}$ (e.g., 32 for $m = 10$), while preserving nearly identical coverage of the achievable $\varepsilon_{r,\mathrm{eff}}$ range. Fig. 3 illustrates the conceptual geometry for the case $m = 10$ using mirror-symmetric stacks selected from the reduced library. Subfigure (a) shows a three-dimensional perspective view of the TO-derived MFE core region, while (b) presents a representative cross-section at $y = 0$, highlighting the uniform layer thickness t and the total height $h = 10t$.

The graded-index distribution in the transverse (x,y) plane is sampled on a uniform square grid. For a design region of extent d discretized by $N_{xy} \times N_{xy}$ sampling points, the lateral pitch is $p = d/(N_{xy} - 1)$. In the present design, $d = 20$ mm and $N_{xy} = 51$, yielding $p = 0.4$ mm, while the vertical discretization is defined by $t = 0.2$ mm. These dimensions lie within the sub-millimeter feature range achievable with low-cost additive-manufacturing techniques for dielectric millimeter-wave structures.

2.4. Discretization and Spatial Assignment of the Modal Effective Index

The spatial assignment process operates on a precomputed library of admissible m-layer configurations, $\mathscr{L}_m \subset \{L,H\}^m$, obtained by enforcing mirror symmetry about the slab mid-plane. Each library entry is characterized by the propagation properties of the fundamental slab-waveguide mode, thereby establishing a direct correspondence between the multilayer geometry and the modal phase velocity.

Within this framework, the continuous TO-derived in-plane distribution is interpreted as a desired spatial variation of the guided mode's effective relative permittivity. For each grid location (x,y), a discrete multilayer configuration is assigned by nearest-neighbor selection in the effective dielectric constant domain. Specifically, the optimal stack $\mathbf{s}^\star(x,y)$ is chosen as

$$\mathbf{s}^\star(x,y) = \arg\min_{\mathbf{s}\in\mathscr{L}_m} \left|\varepsilon_{r,\mathrm{target}}(x,y) - \varepsilon_{r,\mathrm{eff}}(\mathbf{s})\right|, \tag{6}$$

where $\varepsilon_{r,\mathrm{target}}(x,y)$ denotes the target value prescribed by the continuous GRIN profile, and $\varepsilon_{r,\mathrm{eff}}(\mathbf{s})$ is the effective relative permittivity associated with stack configuration $\mathbf{s}$.

The assigned value at each spatial location is then

$$\varepsilon_{r,\mathrm{assigned}}(x,y) = \varepsilon_{r,\mathrm{eff}}\big(\mathbf{s}^\star(x,y)\big), \tag{7}$$

with the local deviation given by

$$\Delta\varepsilon_{r,\mathrm{eff}}(x,y) = \varepsilon_{r,\mathrm{assigned}}(x,y) - \varepsilon_{r,\mathrm{target}}(x,y). \tag{8}$$

This quantity provides a measure of the residual mismatch introduced by the discretized stack assignment. Fig 4 shows the resulting per-pixel assignment for the GRIN region using 32-option mirror-symmetric library. The maximum target effective relative permittivity at the center is $\varepsilon_{r,\mathrm{target}} = 4.0$, compared with the achievable range of 1.82–3.97. The corresponding absolute deviation $|\Delta\varepsilon_{r,\mathrm{eff}}|$ is shown in Fig. 5, indicating that the discretization error remains small over most of the region and increases mainly where the target profile exhibits stronger spatial gradients.

3. Simulation Methodology

The electromagnetic performance of the proposed layered MFE-based crossing is evaluated using full-wave simulations in CST Microwave Studio. The analysis considers transmission characteristics, crosstalk, and modal conversion under excitation of the dominant RDWG mode. The following subsections describe the simulated configuration, the selection of the structure height, the RDWG modal basis, and the power-monitoring strategy used for crosstalk evaluation.

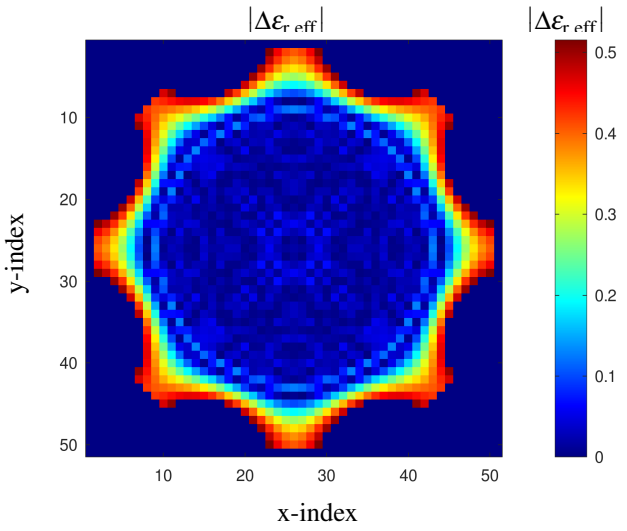


Figure 5: Absolute effective-permittivity error $|\Delta\varepsilon_{r,\mathrm{eff}}|$ at 77 GHz for the GRIN region of Fig. 3, computed as $\left|\varepsilon_{r,\mathrm{assigned}} - \varepsilon_{r,\mathrm{target}}\right|$.

3.1. Simulation Configuration

An example of the simulated eight-port planar waveguide crossing with attached RDWGs is shown in Fig. 6. The central region realizes the TO-derived MFE medium using the layered dielectric model introduced in the previous section. The surrounding RDWGs provide excitation and monitoring access to the crossing region.

The ideal MFE-based N-port crossing may be described by a multiport, multimode scattering matrix whose desired entries correspond to transmission between diametrically opposed ports in the fundamental RDWG mode. All remaining entries correspond to undesired modal conversion or crosstalk and ideally vanish. A complete characterization would therefore require evaluation of the full multimode scattering matrix.

In CST Microwave Studio, waveguide ports are restricted to planar boundaries aligned with the Cartesian coordinate axes, which complicates simultaneous excitation and monitoring of all ports in polygonal crossing geometries such as Fig. 6. Accordingly, an adapted simulation strategy is employed. The ports aligned with the Cartesian axes are modeled explicitly using CST waveguide ports, while the remaining oblique ports are terminated using radiating endfire tips attached to the RDWGs. These terminations provide low-reflection loads and reduce reflections from non-monitored ports during the simulations. For all examples considered in this paper, the return loss of the radiating terminations exceeds 30 dB when $\ell_1 = 10$ mm and $\ell_2 = 5$ mm.

The coordinate system shown in Fig. 6 is used throughout this section: wave propagation occurs along the x-direction, while y and z denote the transverse width and height, respectively.

The corresponding symmetric layered stack used for realization of the crossing region is illustrated in Fig. 7. The structure consists of ten dielectric layers with mirror symmetry about the mid-plane, enabling realization of the required effective-index distribution while maintaining a constant total structure height.

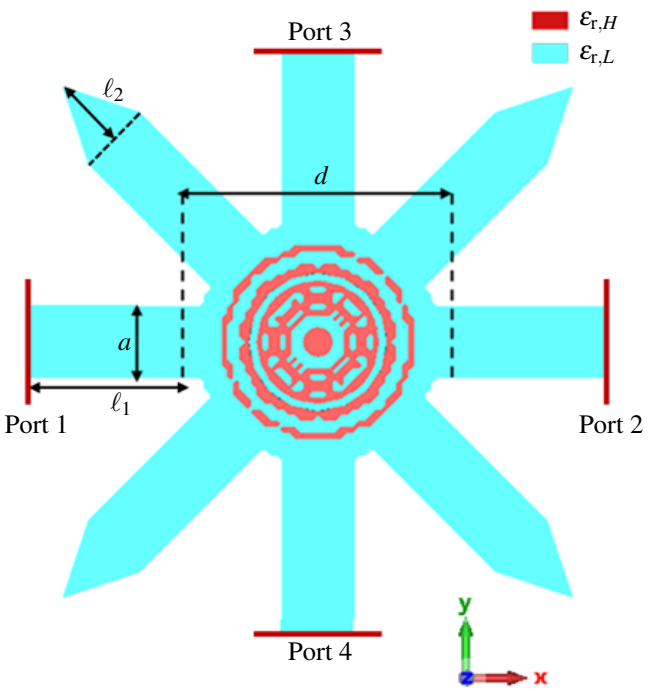


Figure 6: Planar MFE-based 8-port waveguide crossing imported via per-layer DXF; 10-layer cross-section shown in Fig. 7. $\varepsilon_{r,H} = 4.5$, $\varepsilon_{r,L} = 2.2$, $d = 20$ mm, $a = 5$ mm, $h = 2.0$ mm.

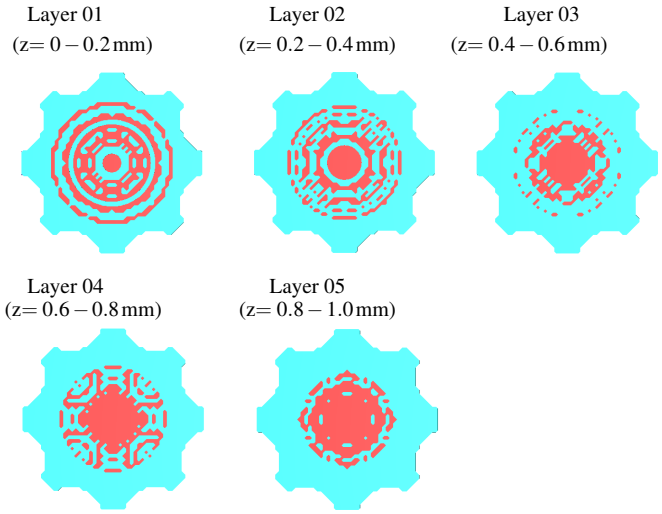


Figure 7: Symmetric stack cross-section used in the waveguide crossing of Fig. 6. Ten layers with five unique slices mirrored about the mid-plane ($1 \leftrightarrow 10$, $2 \leftrightarrow 9$, $3 \leftrightarrow 8$, $4 \leftrightarrow 7$, $5 \leftrightarrow 6$). Per-layer thickness $t = 0.2$ mm.

3.2. Structure Height Selection

The vertical dimension of the layered dielectric structure, denoted by the height h, plays an important role in determining the vertical modal behavior of the crossing region. The choice of h involves a trade-off between field confinement and modal purity. If h is too small, the desired TE_0 slab mode becomes weakly confined and more sensitive to geometrical discontinu-

ities. Conversely, increasing h lowers the cutoff frequencies of additional slab-mode solutions, allowing additional slab modes to propagate at the operating frequency and thereby increasing the risk of modal conversion.

To support the selection of h, the vertical modal behavior of the layered structure is approximated using a three-layer slab model [17]. In the present layered realization, the transformation-optics-derived refractive-index profile is interpreted in terms of the effective refractive index experienced by the guided slab mode rather than the bulk material permittivity itself. The slab-mode analysis therefore provides the effective modal permittivity required to realize the target graded-index distribution.

The analysis is performed for the worst-case permittivity condition occurring near the center of the MFE region, where the local material distribution may approach $\varepsilon_\mathrm{r} = 4.5$. The effective relative permittivity of the slab-mode solutions is therefore evaluated as a function of the slab height h at the operating frequency of 77 GHz.

The resulting dependence is shown in Fig. 8. The three curves correspond to the TE_0, TE_1, and TE_2 slab modes. Only the TE family is considered here, as it corresponds to the polarization of the desired excitation. At the selected height $h = 2$ mm, TE_0 and TE_1 are supported, whereas TE_2 remains below cutoff at 77 GHz. Under idealizing assumptions, the vertical mirror symmetry of the structure with respect to the plane $z = 0$ prevents conversion between modes of opposite symmetry. Thus, the even TE_0 mode does not couple to the odd TE_1 mode, whereas conversion between the even TE_0 and TE_2 modes is in principle possible and can be promoted by the variation of the dielectric constant along the z-direction. Higher-order TE modes have still higher cutoff frequencies and therefore do not constrain the selected height.

In principle, local variations of the structure height could also be used to tailor the effective refractive-index distribution. However, such tapering or thickness modulation would introduce vertical discontinuities and increase fabrication complexity, which is undesirable for the present planar layered realization.

Based on these considerations, the structure height is selected as $h = 2$ mm. In addition to supporting the desired modal behavior, this value is directly compatible with the layered realization of the crossing region, consisting of $m = 10$ dielectric layers with thickness $t = 0.2$ mm.

3.3. RDWG Excitation and Modal Basis

The RDWGs are chosen with the same height as the crossing region in order to avoid additional transitions and maintain a consistent modal environment throughout the structure. The dielectric material of the RDWGs corresponds to the low-permittivity constituent used in the layered MFE realization, with $\varepsilon_{\mathrm{r,L}} = 2.2$. The RDWGs are modeled as dielectric waveguides with height $h = 2$ mm, width $a = 5$ mm, and relative permittivity $\varepsilon_\mathrm{r} = 2.2$.

Selected guided modes supported by the RDWG at the operating frequency of 77 GHz are summarized in Table 1. The mode E_{11}^{y}, adopting Marcatili's notation [18], is used as the excitation mode at the RDWG input ports and serves as the desired transmission mode of the crossing. The additional guided modes listed in Table 1 are considered in order to assess modal conversion and crosstalk. The transverse electric- and magnetic-field distributions of the fundamental RDWG mode E_{11}^{y} at 77 GHz are shown in Fig. 9.

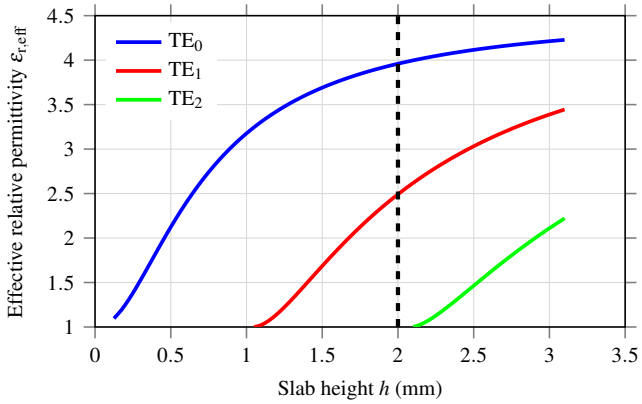


Figure 8: Effective relative permittivity $\varepsilon_{r,\mathrm{eff}}$ of the first three TE slab modes, TE_0, TE_1, and TE_2, as a function of slab height h for $\varepsilon_r = 4.5$ at 77 GHz.

Table 1: Modal properties of the RDWG ($a = 5$ mm, $h = 2$ mm) at 77 GHz.

CST Mode	Mode	f_c (GHz)	n_eff	Pol.
1	E_{11}^{y}	–	1.32	H-pol
2	E_{11}^{z}	–	1.23	V-pol
3	E_{21}^{y}	19.84	1.18	H-pol
4	E_{21}^{z}	30.22	1.12	V-pol

3.4. Crosstalk evaluation

In an ideal MFE-based multiport waveguide crossing, power launched into a given input port is transferred exclusively to the diametrically opposed output port within the desired guided mode. Any power redirected to non-intended ports or converted into higher-order guided modes constitutes crosstalk and should ideally be minimized.

For the eight-port configuration considered here, only the four RDWG ports aligned with the CARTESIAN coordinate axes are modeled explicitly in CST Microwave Studio. The remaining oblique ports are terminated using radiating endfire tips, as discussed in Section 3.1.

Crosstalk and modal conversion are evaluated using the scattering parameters associated with the explicitly modeled RDWG modes. In particular, the transmission coefficient of the fundamental mode between opposing ports is monitored together with scattering parameters associated with higher-order guided modes and non-intended output channels.

Owing to the geometric symmetry of the crossing, undesired power is expected to be distributed approximately symmetrically among equivalent non-intended branches. The resulting scattering-parameter behavior is analyzed in detail in Section 4.

4. Simulation Results and Discussion

The performance of the proposed MFE-based waveguide crossing is evaluated in terms of transmission, reflection, modal

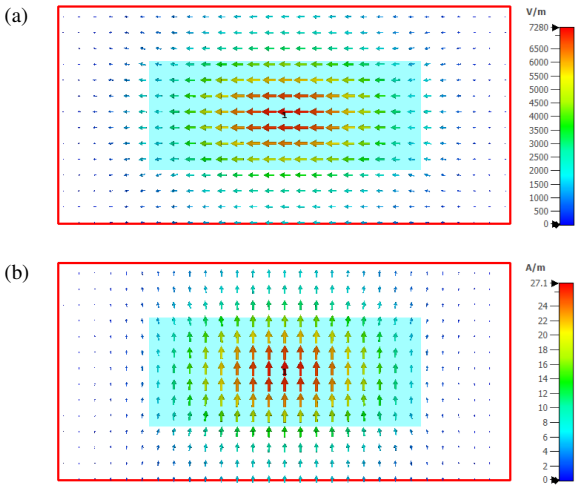


Figure 9: Transverse field distribution of the fundamental mode (E_{11}^{y}) supported by the RDWG with $a = 5$ mm and $h = 2$ mm at 77 GHz. a) Electric field, b) Magnetic field.

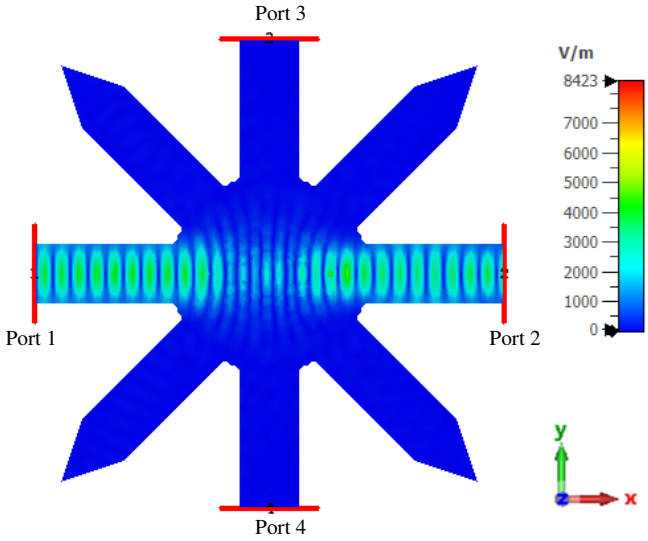


Figure 10: Electric-field magnitude distribution in the waveguide crossing of Fig. 6 at 77 GHz under E_{11}^{y} excitation at Port 1.

conversion, and crosstalk. All results correspond to the layered realization introduced in Fig. 7. The structure is excited at Port 1 using the fundamental mode of the RDWG, E_{11}^{y}, at the operating frequency of 77 GHz, as described in Section 3. The scattering parameters are denoted by $s_{i,j}^{m,n}$, where i and j indicate output and input ports, respectively. The index n denotes the mode of the incoming wave at Port j, while m denotes the mode of the outgoing wave at Port i. The modal indices correspond to those listed in the first column of Table 1.

4.1. Field Distribution

The electric-field magnitude distribution at 77 GHz is shown in Fig. 10. The field is predominantly guided from Port 1 toward the diametrically opposed output port, while only negligible field intensity is observed in the orthogonal branches. This behavior confirms the expected focusing and routing characteristics of the MFE-based design and is consistent with the low magnitudes of the corresponding scattering parameters discussed below. The smooth field evolution through the graded-index region further indicates that no pronounced reflections or abrupt scattering centers are introduced by the layered discretization.

4.2. Scattering Parameters of the Nominal Structure

Figs. 11 and 12 show the transmission and reflection characteristics of the waveguide crossing under excitation of the fundamental RDWG mode E_{11}^{y} at Port 1. The transmission coefficient $|s_{2,1}^{1,1}|$ remains close to 0 dB across the operating band, indicating efficient power transfer between diametrically opposed ports. At the same time, the reflection coefficient $|s_{1,1}^{1,1}|$ has a worst in-band value of approximately -19.1 dB. These results demonstrate that the layered implementation of the MFE-based crossing preserves the intended transmission behavior of the idealized structure.

The guided modes supported by the RDWGs are summarized in Table 1. Although several higher-order and orthogonally polarized modes exist, their excitation under fundamental-mode input remains negligible.

Modal conversion from the fundamental mode is described in terms of the scattering parameters $|s_{2,1}^{m,1}|$ with $m \neq 1$, as shown in Fig. 13. In particular, Fig. 13 shows the conversion from the fundamental E_{11}^{y} mode (Mode 1) to the higher-order E_{21}^{y} mode (Mode 3), with a worst in-band value of approximately -38.7 dB.

Fig. 14 shows the magnitudes of the scattering parameters $|s_{i,1}^{1,1}|$ for $i \in \{3,4\}$ under excitation of the fundamental RDWG mode. While $|s_{2,1}^{1,1}|$ represents the intended transmission path, the scattering parameters $|s_{3,1}^{1,1}|$ and $|s_{4,1}^{1,1}|$ quantify transmission toward non-intended output ports. Across the operating band, these scattering parameters remain well below the desired transmission level, indicating low crosstalk between neighboring branches. Due to the geometric symmetry of the ideal MFE-based crossing, identical responses at Ports 3 and 4 would be expected. The slight asymmetry observed in the simulations is attributed to discretization effects of the layered implementation and polygonal mask generation.

Nevertheless, both $|s_{3,1}^{1,1}|$ and $|s_{4,1}^{1,1}|$ remain below -54 dB at 77 GHz, indicating that the observed asymmetry has no practical impact on the overall device performance. A more symmetric response could be obtained by enforcing additional symmetry constraints during mask generation; however, this was not required for the present design, as the performance remains largely unaffected.

4.3. Effect of Permittivity Thresholding

In the TO-based design, the target permittivity distribution approaches free space ($\varepsilon_{\mathrm{r}} = 1$) near the outer boundary of the polygonal domain. However, the realizable range of effective permittivity is limited by the multilayer implementation. For the considered $m = 10$ layer structure composed of $\varepsilon_{\mathrm{r,H}} = 4.5$

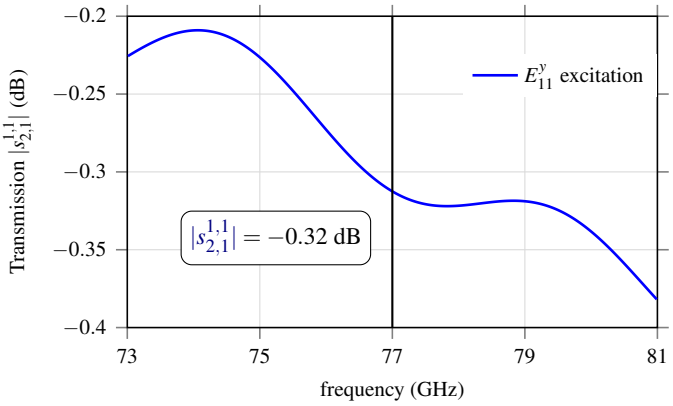


Figure 11: Magnitude of $|s^{1,1}_{2,1}|$ for the waveguide crossing of Fig. 6 under E^y_{11} excitation at Port 1.

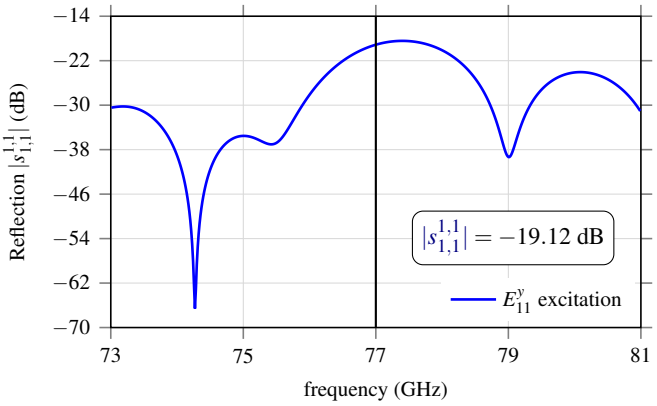


Figure 12: Magnitude of $|s^{1,1}_{1,1}|$ for the waveguide crossing of Fig. 6 under E^y_{11} excitation at Port 1.

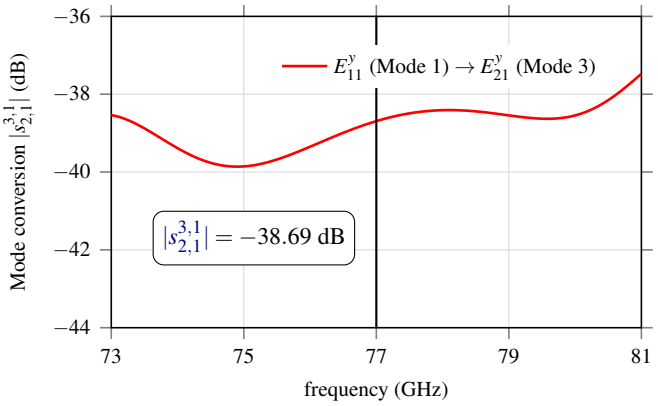


Figure 13: Magnitudes of modal-conversion scattering parameters for the waveguide crossing of Fig. 6 under E^y_{11} excitation at Port 1.

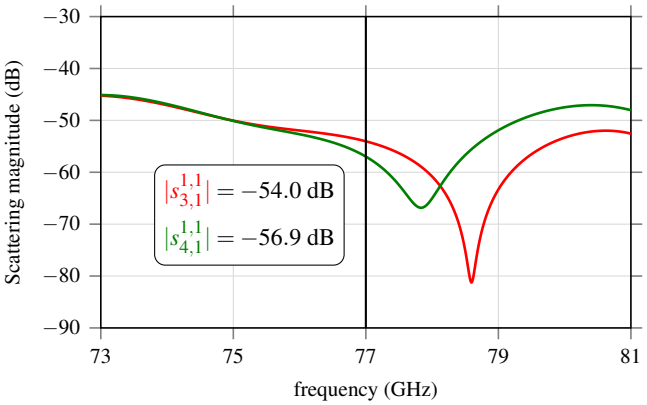


Figure 14: Magnitudes of $|s^{1,1}_{3,1}|$ and $|s^{1,1}_{4,1}|$ for the waveguide crossing of Fig. 6 under E^y_{11} excitation at Port 1, representing crosstalk toward non-intended output ports.

and $\varepsilon_{r,L} = 2.2$, the minimum achievable effective permittivity is approximately 1.82. As a consequence, enforcing the target distribution in regions where $\varepsilon_{r,target} \to 1$ introduces a systematic mismatch between the desired and realizable values. This mismatch is most pronounced near the outer boundary of the transformed domain. At the same time, the electromagnetic field is predominantly concentrated in regions of higher effective permittivity, where stronger confinement occurs and most of the transmitted power is carried.

Based on this observation, a threshold is introduced such that only regions satisfying

$$\varepsilon_{r,target}(x,y) > \varepsilon_{r,th}$$

are retained, while regions below this threshold are excluded. This truncates boundary regions with limited influence on the dominant propagation paths.

Fig. 15 shows the thresholded boundaries for different values of $\varepsilon_{r,th}$. The geometry corresponding to $\varepsilon_{r,th} = 1.3$ matches the reference design shown in Fig. 6 and is used as the baseline configuration in the following. Increasing the threshold progressively removes outer regions associated with lower effective permittivity. The choice $\varepsilon_{r,th} = 1.3$ represents a compromise between geometric fidelity and electromagnetic performance. This value is also consistent with the midpoint estimate obtained from the corresponding local phase velocities of free space and the minimum realizable effective permittivity ($\varepsilon_{r,eff} \approx 1.82$), which yields an equivalent transition value of approximately $\varepsilon_{r,eff} \approx 1.32$. This is further confirmed by the transmission results shown in Fig. 16, where the scattering parameter $|s^{1,1}_{2,1}|$ is compared for different threshold values. Despite the noticeable geometric differences illustrated in Fig. 15, the transmission response remains largely unchanged across the considered threshold range. This indicates that truncation of low-permittivity boundary regions has only minor influence on the dominant propagation path, since the electromagnetic field is concentrated primarily within the higher-permittivity core region.

Alternative approaches, such as introducing air as an additional material or employing tapered height variations, were also considered. However, these approaches increase fabrication complexity and may introduce additional scattering due to material or geometrical discontinuities. The thresholding strategy therefore provides a simple and robust means of approximating the target distribution while preserving the planar layered realization. These results confirm that the proposed trun-

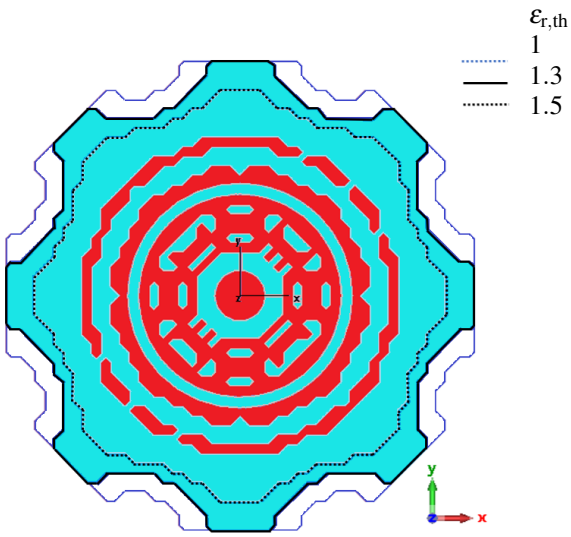


Figure 15: Boundaries of the thresholded layouts for a fixed nominal diameter $d = 20\,\text{mm}$, obtained for different effective-permittivity thresholds $\varepsilon_{r,th}$.

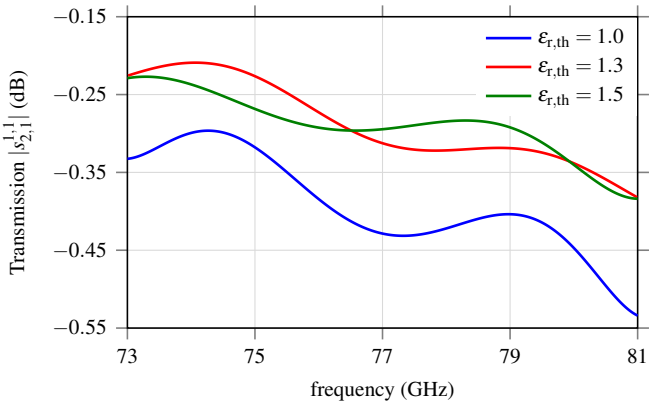


Figure 16: Transmission coefficient $|s^{1,1}_{2,1}|$ for different effective-permittivity thresholds $\varepsilon_{r,th}$.

cation strategy provides a robust approximation of the target distribution without requiring realization of the full transformed-domain extent.

4.4. Influence of Structural Parameters on Loss

To assess practical applicability, dielectric losses are included in the simulations. The material parameters are based on commercially available ceramic filaments (e.g., Zetamix [19]), with a nominal loss tangent of $\tan\delta \approx 1 \times 10^{-3}$. To account for uncertainties in material characterization and operation at higher frequencies, an increased value of $\tan\delta = 0.002$ is additionally considered.

Fig. 17 shows the transmission coefficient $|s^{1,1}_{2,1}|$ for different lens diameters and dielectric loss factors. In the lossless case, larger diameters improve transmission performance by increasing the electrical size of the crossing relative to the free-space wavelength, thereby providing propagation conditions that more closely approach those assumed by the underlying MFE model.

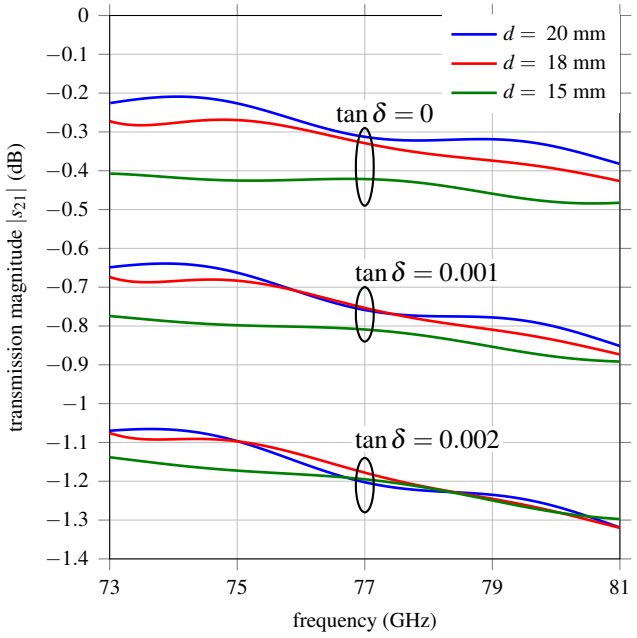


Figure 17: Transmission magnitude $|s_{21}|$ for the waveguide crossing after Fig. 6 for different sizes and dielectric loss factors when fed at port 1 with fundamental mode after Fig. 9.

In the presence of dielectric loss, however, larger structures lead to longer propagation paths and consequently increased attenuation. This illustrates the trade-off between improved modal guidance associated with increased electrical size and the additional dielectric attenuation introduced by longer propagation distances. The results therefore indicate that the preferred lens diameter depends on the balance between transmission performance and dielectric-loss-induced attenuation. The reference design used throughout this work employs $d = 20$ mm.

4.5. Impact of a Shielding Enclosure

While the previous results were obtained under idealized free-space conditions, a more practical configuration is now considered. In experimental implementations, mechanical support and electromagnetic shielding are typically required to ensure stable operation and reproducible measurements.

Accordingly, the waveguide crossing is enclosed by two parallel metallic plates, positioned symmetrically above and below the dielectric structure at a distance h_c from its upper and lower surfaces, respectively, as illustrated in Fig. 18. The plates are modeled as perfect electric conductor (PEC) surfaces. The lateral extent of the PEC plates is chosen to cover the MFE and a short section of each connected RDWG only, excluding the radiating tips which substitute for terminations only for purposes of simulation. The separation distance h_c influences the modal behavior of the enclosed structure. If h_c is too large, additional parallel-plate or higher-order modes may be supported. Conversely, if h_c becomes too small, the assumptions underlying the original free-space design are increasingly violated. A parametric study of h_c is presented in Figs. 19 and 20. For the investigated values $h_c = 0.6$, 0.7, and 0.9 mm, the results show smooth transmission and reflection characteristics over

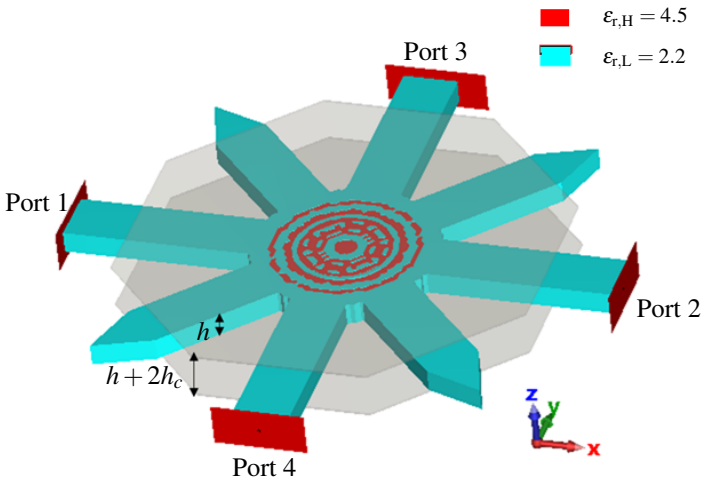


Figure 18: Waveguide crossing of Fig. 6 enclosed between two parallel PEC plates, positioned at a distance h_c from the upper and lower surfaces of the dielectric structure.

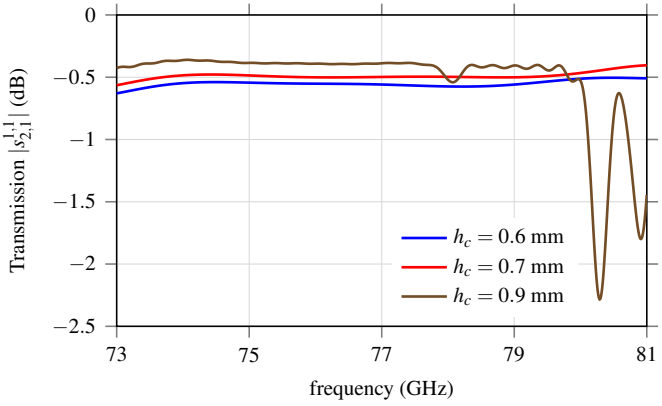


Figure 19: Transmission coefficient $|s_{2,1}^{1,1}|$ of the waveguide crossing enclosed between parallel PEC plates (Fig. 18) under E_{11}^{y} excitation at Port 1, for $h_c \in \{0.6, 0.7, 0.9\}$ mm.

the considered frequency range.

The presence of the PEC plates modifies the modal propagation characteristics. The dominant mode follows the same overall routing path as in the free-space case, but with an increased propagation constant β, indicating stronger field confinement within the dielectric region. Compared with the free-space configuration, the enclosed structure exhibits comparable, and in some cases slightly improved, transmission performance, while the crosstalk levels $|s_{3,1}^{1,1}|$ and $|s_{4,1}^{1,1}|$ remain low. These results confirm that the proposed layered MFE-based waveguide crossing can be implemented within a practically enclosed configuration without significant degradation of performance.

5. Conclusion

A transformation-optics-based modal-domain methodology for realizing graded-index designs in planar layered dielectric waveguide structures has been presented. By expressing the design target in terms of the effective relative permittivity of the fundamental guided slab mode, the approach enables direct realization using manufacturable multilayer stacks composed of

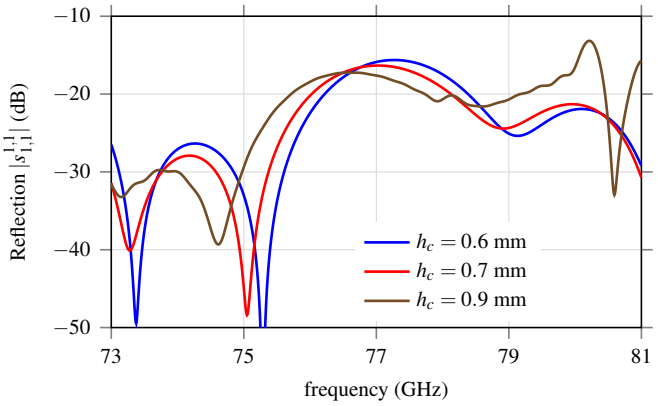


Figure 20: Reflection coefficient $|s_{1,1}^{1,1}|$ of the waveguide crossing enclosed between parallel PEC plates (Fig. 18) under E_{11}^{y} excitation at Port 1, for $h_c \in \{0.6, 0.7, 0.9\}$ mm.

two low-loss dielectric materials, without requiring a prescribed bulk permittivity distribution.

The method was demonstrated for a Maxwell's fish-eye multiport waveguide crossing operating in the 77 GHz automotive radar band. A reduced library of mirror-symmetric layer stacks provides near-continuous coverage of the required effective-permittivity range, enabling accurate spatial discretization while maintaining constant slab thickness. Full-wave simulations confirm high transmission, low reflection, low modal conversion, and low crosstalk toward non-intended output ports. In addition, the design exhibits robustness with respect to dielectric loss, boundary truncation, and practical metallic enclosure conditions.

The developed framework is applicable to a broader class of guided-wave devices derived from transformation-optics concepts and establishes a systematic, fabrication-compatible route toward compact, low-loss millimeter-wave dielectric interconnects and functional components for future high-frequency systems.

References

[1] C. Waldschmidt, J. Hasch, and W. Menzel, "Automotive radar – from first efforts to future systems," *IEEE Journal of Microwaves*, vol. 1, no. 1, pp. 135–148, 2021.

[2] Z. Zang, Q. Ren, A. Uz Zaman, and J. Yang, "77 GHz fully polarimetric antenna system with compact circularly polarized slots in gap waveguide for automotive radar," *IEEE Transactions on Antennas and Propagation*, vol. 72, no. 7, pp. 5578–5588, 2024.

[3] L. C. Van Atta, "Electromagnetic reflector," US Patent 2,908,002, Oct., 1959.

[4] A. A. M. Ali, H. B. El-Shaarawy, and H. Aubert, "Millimeter–wave substrate integrated waveguide passive Van Atta reflector array," *IEEE Transactions on Antennas and Propagation*, vol. 61, no. 3, pp. 1465–1470, 2013.

[5] H.-B. Zhan, X.-C. Li, C.-S. Sun, K. Ning, and J.-F. Mao, "A low-loss power dividing transition from microstrip line

to two rectangular dielectric waveguides at w-band," *IEEE Transactions on Microwave Theory and Techniques*, pp. 1–11, 2026.

[6] H. Xu and Y. Shi, "Metamaterial-based Maxwell's fish-eye lens for multimode waveguide crossing," *Laser and Photonics Reviews*, vol. 12, 08 2018.

[7] S. H. Badri, H. Rasooli Saghai, and H. Soofi, "Polygonal Maxwell's fisheye lens via transformation optics as multimode waveguide crossing," *Journal of Optics*, vol. 21, no. 6, p. 065102, 2019.

[8] J. Maxwell and W. Niven, *The Scientific Papers of James Clerk Maxwell*, ser. Dover Phoenix Editions. Dover Publications, 2003, vol. 1.

[9] N. Messhenas, W. L. Schroeder, and T. Kaiser, "Assessment of mfe-based multiport waveguide crossing for use with low-cost, low-loss dielectric interconnects in millimeter wave arrays," in *2024 18th European Conference on Antennas and Propagation (EuCAP)*, 2024, pp. 1–5.

[10] ——, "Transformation-optics-based modal-domain realization of a layered Maxwell Fish–Eye multiport waveguide crossing at 77 GHz," in *20th European Conference on Antennas and Propagation (EuCAP)*, 2026.

[11] S. Li, Y. Zhou, J. Dong, X. Zhang, E. Cassan, J. Hou, C. Yang, S. Chen, D. Gao, and H. Chen, "Universal multimode waveguide crossing based on transformation optics," *Optica*, vol. 5, no. 12, pp. 1549–1556, 2018.

[12] J. B. Pendry, D. Schurig, and D. R. Smith, "Controlling electromagnetic fields," *Science*, vol. 312, pp. 1780–1782, 2006.

[13] U. Leonhardt, "Optical conformal mapping," *Science*, vol. 312, no. 5781, pp. 1777–1780, 2006.

[14] H. Eskandari, M. S. Majedi, A. R. Attari, and O. Quevedo-Teruel, "Elliptical generalized Maxwell fish-eye lens using conformal mapping," *New Journal of Physics*, vol. 21, no. 6, p. 063010, 2019.

[15] L. N. Trefethen, "Numerical computation of the schwarz—christoffel transformation," *SIAM Journal on Scientific and Statistical Computing*, vol. 1, no. 1, pp. 82–102, 1980.

[16] A. Pitilakis, "MLSWG: Frequency-domain vector mode solver for multi-layer slab waveguides," https://github.com/alexpiti/MLSWG.

[17] S. J. Orfanidis, *Electromagnetic Waves and Antennas*. Orfanidis, 2016.

[18] E. Marcatili, "Dielectric rectangular waveguide and directional coupler for integrated optics," *Bell System Technical Journal*, vol. 48, no. 7, pp. 2071–2102, 1969.

[19] Nanoe, "Zetamix ε high permittivity materials for 3d printing," 2022. [Online]. Available: https://zetamix.fr/en/produit/zetamix-%C9%9B-filament/